Real Space Imaging of the Atomic-Scale Magnetic Structure of $\mathrm{Fe}_{1+y}\mathrm{Te}$

Mostafa Enayat,[1,*] Zhixiang Sun,[1,*] Udai Raj Singh,[1] Ramakrishna Aluru,[1]

Stefan Schmaus,[1] Alexander Yaresko,[1] Yong Liu,[1,†] Chengtian Lin,[1]

Vladimir Tsurkan,[2,3] Alois Loidl,[2] Joachim Deisenhofer,[2] and Peter Wahl[1,4,‡]

[1]*Max-Planck-Institut für Festkörperforschung,*

Heisenbergstr. 1, D-70569 Stuttgart, Germany

[2]*Center for Electronic Correlations and Magnetism, Experimental Physics V,*

University of Augsburg, D-86159 Augsburg, Germany

[3]*Institute of Applied Physics, Academy of Sciences*

of Moldova, MD 2028, Chisinau, R. Moldova

[4]*SUPA, School of Physics and Astronomy,*

University of St. Andrews, North Haugh,

St. Andrews, Fife, KY16 9SS, United Kingdom

(Dated: April 29, 2014)

Abstract

High temperature superconductivity, both in cuprate as well as iron pnictide materials, occurs in close proximity to magnetically ordered phases, indicating an intimate relationship between the two. While the undoped parent compounds often exhibit antiferromagnetic order, commensurate with the crystal lattice, at increased doping, more complex, often incommensurate, magnetic orders have been detected. Up to now, most information on the magnetic structure of strongly correlated electron systems has been obtained by neutron scattering. Here we demonstrate real space atomic scale imaging of the magnetic structure of iron tellurium ($\mathrm{Fe}_{1+y}\mathrm{Te}$), the non-superconducting parent compound of the iron chalcogenides, by low temperature scanning tunneling microscopy. Our images of the magnetic structure reveal that magnetic order in the monoclinic phase is truly a unidirectional stripe order, whereas in the orthorhombic phase at higher excess iron concentration ($y > 0.12$), a transition to a phase with coexistence of magnetic order in both directions, locally reminiscent of a plaquette order, is observed.

*These authors contributed equally.

†Present address: Division of Materials Sciences and Engineering, Ames Laboratory, US DOE, Ames, Iowa 50011, USA

‡Electronic address: gpw2@st-andrews.ac.uk

A recurring theme in strongly correlated high temperature superconductors is that a non-superconducting parent compound, which is in an antiferromagnetically ordered state, becomes superconducting upon doping the material. This is true for most of the iron-based high temperature superconductors (HTSC) (*1–3*) and for copper-oxide based materials (*4*). Establishing the relation between magnetic order and superconductivity is believed to be key to understanding the physics and the mechanism of high temperature superconductivity in these materials. Magnetic order in strongly correlated electron materials is usually obtained by neutron scattering, where it shows up as magnetic scattering peaks. Real space imaging of magnetic order is possible with spin-polarized scanning tunneling microscopy (SP-STM), which has been used extensively to study magnetic properties of thin films, nanostructures and magnetic clusters (*5–7*). Despite its potential, especially for visualizing the transition from the magnetically ordered parent compound to the superconducting state, characterization of atomic scale magnetic structure in strongly correlated electron materials and, in particular, materials relevant for high temperature superconductivity has not been achieved so far by SP-STM (*7*).

$\mathrm{Fe}_{1+y}\mathrm{Te}$ is the non-superconducting parent compound of the iron chalcogenide superconductors, in which superconductivity is induced by substitution of Te by Se (*8*). The parent compound exhibits a bicollinear stripe magnetic order with a wave vector $(1/2, 0, 1/2)$ (defined in the two iron unit cell, see Fig. 1A) (*9–11*). Magnetic order sets in at a temperature of around $60 - 70$ K, accompanied by a structural phase transition, with the structure changing from tetragonal to monoclinic. With increasing concentration y of excess iron, the transition temperature is reduced and the magnetic and structural transitions are separated (*12*, *13*). At excess iron concentrations $y > 0.12$, the crystal structure becomes orthorhombic (*13*) and the magnetic order becomes incommensurate with the lattice (*11*). The magnetic structure is remarkably different from the one found in the parent compounds of the iron-pnictide superconductors. The absence of nesting at the wave vector of the magnetic order suggests that local moments and

their interactions are important. Due to their layered structure, electronic properties and magnetism in iron-based materials are quasi two-dimensional (*3*) — making them ideally suited for a study by SP-STM. Because the magnetic interactions in iron tellurium are predominantly two-dimensional within the FeTe-plane, in the following only the in-plane component of the magnetic order will be considered. The experimental challenge lies in identifying a suitable procedure for preparing an STM tip which yields magnetic contrast.

While DFT calculations reproduce the magnetic structure at $y = 0$ (*14*, *15*), mapping onto a Heisenberg model remains controversial(*16*). Different microscopic Heisenberg models have been proposed to describe the magnetic order in the FeTe plane and the spin excitations: Heisenberg models including up to third nearest neighbour interactions (*15*, *17*, *18*) capture the bicollinear spin order (*10*, *11*), whereas accounting for quantum fluctuations favors spin plaquettes of four nearest neighbour iron atoms (*19*, *20*).

In this paper, we report an investigation by SP-STM of the real space magnetic structure at the atomic scale of the non superconducting parent compound, $\mathrm{Fe}_{1+y}\mathrm{Te}$, of the iron chalcogenide superconductors. Our data, obtained with a tip which has a magnetic cluster at its apex (see Fig. 1B), reveals a unidirectional bicollinear magnetic stripe order at low excess iron concentration y and a transition towards bidirectional incommensurate magnetic order at high excess iron concentrations $y > 0.12$.

$\mathrm{Fe}_{1+y}\mathrm{Te}$ has a layered crystal structure in which the iron chalcogenide layers are only weakly bound by van-der-Waals interactions, yielding natural cleavage planes. A topographic image of the sample surface with atomic resolution is shown in Fig. 1C. The square lattice can be identified from its lattice constant as the top layer tellurium atoms. Excess iron atoms at the surface show up as bright protrusions (*21–23*). The Fourier transform of the topography clearly shows the peaks associated with the tellurium lattice at the surface. The two non-equivalent spots as-

sociated with the tellurium lattice at $\mathbf{q}^a_{\mathrm{Te}} = (\pm 1, 0)$ and $\mathbf{q}^b_{\mathrm{Te}} = (0, \pm 1)$ have noticeably different intensities. A topographic image obtained in the same place as the one in Fig. 1C with a tip which yields magnetic contrast is shown in Fig. 1D. It shows clear stripe-like patterns superimposed to the atomic lattice. The stripes are due to spin-polarized tunneling into regions with a spin-polarization parallel or antiparallel to that of the tip, imaged higher or lower, respectively. The Fourier transform of the topography reveals an additional pair of peaks with half the wave vector compared to the atomic peaks (compare also sketch in Fig. 1A). The unidirectional modulation has two major components in the Fourier transform: the first is a pair of distinct peaks at wave vectors $\mathbf{q}_{\mathrm{AFM}} = (\pm 1/2, 0)$, the second, which is also seen with a non-magnetic tip, at $\mathbf{q}_{\mathrm{CDW}} = (\pm 1, 0)$ coincides with the atomic peak of the tellurium lattice – and is still clearly noticeable by the intensity difference compared to the other peak related to the Te lattice ($\mathbf{q}^b_{\mathrm{Te}} = (0, \pm 1)$). Antiferromagnetic or spin density wave (SDW) order is expected to be accompanied by a charge density wave (CDW) (*24*, *25*) with twice the wave vector of the magnetic order (i.e. $\mathbf{q}_{\mathrm{CDW}} = 2\mathbf{q}_{\mathrm{AFM}}$), consistent with our data. A superposition of a sketch of the magnetic structure with a topographic image is shown in Fig. 1E. The modulation due to the antiferromagnetic order was observed consistently over large surface areas and was never found to switch direction within a domain of the monoclinic distortion in samples with low excess iron concentration ($y < 0.12$) — only at domain boundaries do the stripes switch direction (Fig. 1F).

Calculations (details see Suppl. Mat. S1E, Fig. S2) show that besides the Fe atoms, also the electronic states at the Te sites are strongly spin-polarized in the vicinity of the Fermi level, with the direction of the induced magnetization of the Te atoms being in plane and in opposite direction to the spin of the three equal-spin iron neighbours. Based on the topographic contrast (up to $\sim 20\mathrm{pm}$ between equivalent sites), the spin-polarization of the tunneling current is up to 20%. This would be consistent with the spin-polarization found on either the iron or tellurium atoms in the calculation and that of an iron-coated tip (*26*). The magnetic peaks we observe at

$\mathbf{q}_{\mathrm{A}FM}$ likely contain contributions from both.

To verify that the stripe modulation originates from spin-polarized tunneling, we have performed measurements in magnetic field. Fig. 2A and B show topographic images taken at the same location on the surface in magnetic fields of $B = +5\mathrm{T}$ and $-5\mathrm{T}$, respectively. The stripes shift by half the wave length of the antiferromagnetic order on reversing the direction of the magnetic field. This can be clearly seen in the line profiles in the upper panel of Fig. 2C which have been obtained from Fig. 2A and B by averaging along the stripes of the modulation (parallel to b), resulting in a profile of the modulation along a. The magnetic field dependence of the imaging contrast demonstrates that the stripe modulation is due to spin-polarized tunneling. Because the sample has only a small net magnetization, the magnetic field switches the magnetization of the tip only.

The atomic registry of the topographies in Fig. 2A, B allows us to separate magnetic from topographic information and extract the spin polarization of the tunneling current (see Suppl. Mat. S2). The average of the two images yields a spatial map of the non-magnetic contrast (black line in lower panel of Fig. 2C, map in Fig. 2D), whereas the difference yields the magnetic contrast only (red line in lower panel of Fig. 2C, map in Fig. 2E). Close inspection of the line profiles in Fig. 2C reveals that the strongest spin polarization is observed in between the tellurium atoms. Hence the dominant contribution to the magnetic contrast comes from direct tunneling to the iron d-states.

The appearance of excess iron atoms shows a strong dependence on the spin-polarization of the tip, as can be seen from Fig. 2A, B and the line cut shown in Fig. 2F. The topographic height of the excess iron atoms is directly correlated with the apparent height of the trough between two rows of Tellurium atoms, both switching their apparent height with field. Line cuts through two defects with opposite spin polarization are plotted in the upper panel of Fig. 2F, one imaged high and the other low at $5\mathrm{T}$ and vice versa at $-5\mathrm{T}$. Assuming that for both tunneling occurs

predominantly into a minority state, the spin of the excess iron atoms is parallel to the one of its three equal-spin neighbours (compare Fig. 2G). This is confirmed by DFT calculations, which show that this configuration is the energetically favourable one and the states at the Fermi energy are predominantly of minority character (see Suppl. Mat. S1E, fig. S3). A plot of the spin polarization across the two excess iron atoms (Fig. 2F, lower panel) shows that the magnetic contrast found on and near excess iron atoms is enhanced.

While our data at low temperature shows the same periodicity of the magnetic order as found in neutron scattering, in order to establish its relation to the magneto-structural phase transition observed in the bulk we studied its temperature dependence. On increasing the temperature, the stripe modulation disappeared around a temperature T of 45 K and was not observed at $T > 50$ K. A topographic image taken at $T = 54$ K is displayed in Fig. 3A. The Fourier transform (inset in Fig. 3A) shows only the peaks associated with the Te lattice. To quantify the intensity of the modulation, we used the ratio $\Psi_{\mathrm{AFM}} = \widetilde{z}(\mathbf{q}_{\mathrm{AFM}})/\widetilde{z}(\mathbf{q}^b_{\mathrm{Te}})$ of the amplitude of the Fourier component at the wave vector of the magnetic order $\widetilde{z}(\mathbf{q}_{\mathrm{AFM}})$ with the amplitude of the (weaker) atomic peak $\widetilde{z}(\mathbf{q}^b_{\mathrm{Te}})$. Figure 3B shows the temperature dependence of Ψ_{AFM}. The trend is consistent with a mean-field behavior with a critical temperature $T_{\mathrm{c}} = 45$ K (solid line in Fig. 3B). *A priori* it is not clear whether the disappearance of the magnetic contrast is related to the transition to the paramagnetic phase of the sample or due to a loss of spin-polarization of the tip. This can be clarified by analyzing the CDW modulation which accompanies the antiferromagnetic order which is also detected with a non-magnetic tip. In Fig. 3C, we plot Ψ_{CDW} as a measure for the intensity of the peak at $\mathbf{q}_{\mathrm{CDW}} = \mathbf{q}^a_{\mathrm{Te}}$ as a function of temperature. The asymmetry of the intensity of the atomic peaks shows the same temperature dependence as the intensity of the peak at $\mathbf{q}_{\mathrm{AFM}}$, therefore it is really the magnetic order of the sample which is suppressed. The transition temperature in the bulk ($60 - 70$ K) is somewhat larger. A possible reason for this is that the surface iron-tellurium layer has only one neighbouring layer

as opposed to two in the bulk.

The magnetic order in $\mathrm{Fe}_{1+y}\mathrm{Te}$ becomes more complex with increased excess iron content y (*11*, *27*). Figure 4A shows a topographic image obtained on a sample with higher excess iron concentration (at $y = 0.15$). In contrast to measurements taken on samples with lower excess Fe concentration, the topography reveals stripe-like patterns in both directions, i.e. at $(\pm 1/2, 0)$ and $(0, \pm 1/2)$ in Fourier space (inset of Fig. 4A), coexisting in the same domain of the orthorhombic distortion. The image reveals nanoscale domains of predominantly unidirectional stripes coexisting with regions of bidirectional patterns. These two-dimensional patterns could be due to a superposition between the two unidirectional modulations or due to a transition towards a plaquette order, which has been theoretically predicted to become more important due to quantum fluctuations as the sample becomes orthorhombic (*20*). As can be seen from the real space picture, the magnetic structure is still locally commensurate with the lattice, however, there are phase slips between different nanoscale domains. This can be more clearly seen from a Fourier-filtered image where only the Fourier components associated with the magnetic contrast are shown (Figure 4B).

The picture which emerges from our measurements is that at low excess iron concentrations, the magnetic order is commensurate and locked with the monoclinic distortion of the lattice. In Heisenberg models incorporating interactions up to the third nearest neighbour, this has been rationalized by anisotropic coupling between nearest and next-nearest neighbour iron spins (*17*) or by the influence of orbital ordering on the magnetic couplings (*18*). Our observation of a unidirectional stripe-like magnetic order in the monoclinic phase indicates that the monoclinic distortion suppresses bidirectional or plaquette magnetic order at low excess iron concentrations, strongly favouring unidirectional stripe order. As the lattice constants in the a- and b-direction approach each other with increasing excess Fe concentration (*11*, *28*), we observe both directions of the magnetic order near $(1/2, 0)$ and $(0, 1/2)$ coexisting in the same

domain of the sample with patches reminiscent of plaquette order. Further, the magnetic order becomes incommensurate. Non-commensurate magnetic order has also been detected in neutron scattering at high excess iron concentrations, showing a shortening of the wave vector associated with the magnetic order (*11*, *27*). In our case the peak associated with the magnetic order spreads away from the high symmetry direction. As the material still has an orthorhombic distortion, the two directions will not have the same energetics. This raises interesting questions as to how the magnetic order sets in as a function of temperature. For certain excess iron concentrations, there is evidence from neutron scattering and x-ray diffraction for an additional magnetically ordered phase at higher temperatures (*13*, *27*).

In summary, we have carried out spin-polarized low temperature STM experiments on $\mathrm{Fe}_{1+y}\mathrm{Te}$ crystals with iron concentrations from $y = 0.08$ to 0.15 to characterize the atomic scale spin structure by spin-polarized tunneling. We found a commensurate unidirectional stripe modulation at low excess iron concentration, with a transition to coexistence of the two almost equivalent directions of the stripe order and patches reminiscent of plaquette order at larger excess iron concentrations. The observation of magnetic structures on the atomic scale in parent compounds of high temperature superconductors brings the possibility into reach to obtain real space images of stripe order in cuprates (*29–31*) and search for magnetic order accompanying the spatially modulated electronic states found in the pseudogap phase(*32*, *33*).

---

1. K. Ishida, Y. Nakai, and H. Hosono. To what extent Iron-pnictide new superconductors have been clarified: A progress report. *J. Phys. Soc. Jpn.*, 78(6):062001, (2009).
2. J. Paglione and R.L. Greene. High-temperature superconductivity in iron-based materials. *Nat. Phys.*, 6(9):645–658, (2010).
3. M.D. Lumsden and A.D. Christianson. Magnetism in Fe-based superconductors. *J. Phys.: Condens. Matter*, 22(20):203203, (2010).

4. E. Dagotto. Complexity in strongly correlated electron systems. *Science*, 309:257–262, (2005).
5. R. Wiesendanger, H.-J. Güntherodt, G. Güntherodt, R.J. Gambino, and R. Ruf. Observation of vacuum tunneling of spin-polarized electrons with the scanning tunneling microscope. *Phys. Rev. Lett.*, 65:247–250, (1990).
6. A.R. Smith. Atomic-scale spin-polarized scanning tunneling microscopy and atomic force microscopy: A review. *Jrnl. Scan. Prob. Micr.*, 1:3–20, (2006).
7. R. Wiesendanger. Spin mapping at the nanoscale and atomic scale. *Rev. Mod. Phys.*, 81:1495–1550, (2009).
8. Y. Mizuguchi and Y. Takano. Review of Fe chalcogenides as the simplest Fe-based superconductor. *J. Phys. Soc. Jpn.*, 79(10):102001, (2010).
9. D. Fruchart, P. Convert, P. Wolfers, R. Madar, J.P. Senateur, and R. Fruchart. Structure antiférromagnetique de $\mathrm{Fe_{1.125}Te}$ accompagnée d'une déformation monoclinique. *Mat. Res. Bull.*, 10:169–174, (1975).
10. S. Li, C. de la Cruz, Q. Huang, Y. Chen, J.W. Lynn, J. Hu, Y.L. Huang, F.C. Hsu, K.W. Yeh, M.K. Wu, and P. Dai. First-order magnetic and structural phase transitions in $\mathrm{Fe_{1+y}Se_xTe_{1-x}}$. *Phys. Rev. B*, 79:054503, (2009).
11. W. Bao, Y. Qiu, Q. Huang, M.A. Green, P. Zajdel, M.R. Fitzsimmons, M. Zhernenkov, S. Chang, M. Fang, B. Qian, E.K. Vehstedt, J. Yang, H.M. Pham, L. Spinu, and Z.Q. Mao. Tunable ($\delta\pi$, $\delta\pi$)-type antiferromagnetic order in α-Fe(Te, Se) superconductors. *Phys. Rev. Lett.*, 102(24):247001, (2009).
12. A. Martinelli, A. Palenzona, M. Tropeano, C. Ferdeghini, M. Putti, M.R. Cimberle, T.D. Nguyen, M. Affronte, and C. Ritter. From antiferromagnetism to superconductivity in $\mathrm{Fe_{1+y}Te_{1-x}Se_x}$: Neutron powder diffraction analysis. *Phys. Rev. B*, 81(9):094115, (2010).
13. S. Rößler, D. Cherian, W. Lorenz, M. Doerr, C. Koz, C. Curfs, Y. Prots, U.K. Rößler, U. Schwarz, S. Elizabeth, and S. Wirth. First-order structural transition in the magnetically ordered phase of $\mathrm{Fe_{1.13}}$ Te. *Phys. Rev. B*, 84(17):174506, (2011).
14. M.D. Johannes and I.I. Mazin. Microscopic origin of magnetism and magnetic interactions in ferropnictides. *Phys. Rev. B*, 79:220510, (2009).

15. F. Ma, W. Ji, J. Hu, Z.Y. Lu, and T. Xiang. First-principles calculations of the electronic structure of tetragonal α-FeTe and α-FeSe crystals: evidence for a bicollinear antiferromagnetic order. *Phys. Rev. Lett.*, 102(17):177003, (2009).

16. J.K. Glasbrenner, J.P. Velev, and I.I. Mazin. First-principles study of the minimal model of magnetic interactions in Fe-based superconductors. *Phys. Rev. B*, 89:064509, (2014).

17. C. Fang, B.A. Bernevig, and J. Hu. Theory of magnetic order in $Fe_{1+y}Se_xTe_{1-x}$. *Europhys. Lett.*, 86:67005, (2009).

18. A.M. Turner, F. Wang, and A. Vishwanath. Kinetic magnetism and orbital order in iron telluride. *Phys. Rev. B*, 80(22):224504, (2009).

19. I.A. Zaliznyak, Z. Xu, J.M. Tranquada, G. Gu, A.M. Tsvelik, and M.B. Stone. Unconventional temperature enhanced magnetism in $Fe_{1.1}Te$. *Phys. Rev. Lett.*, 107(21):216403, (2011).

20. S. Ducatman, N.B. Perkins, and A. Chubukov. Magnetism in parent Fe-chalcogenides: quantum fluctuations select a plaquette order. *Phys. Rev. Lett.*, 109:157206, (2012).

21. X.B. He, G.R. Li, J.D. Zhang, A.B. Karki, R.Y. Jin, B.C. Sales, A.S. Sefat, M.A. McGuire, D. Mandrus, and E.W. Plummer. Nanoscale chemical phase separation in $FeTe_{0.55}Se_{0.45}$ as seen via scanning tunneling spectroscopy. *Phys. Rev. B*, 83:220502, (2011).

22. T. Machida, K. Kogure, T. Kato, H. Nakamura, H. Takeya, T. Mochiku, S. Ooi, Y. Mizuguchi, Y. Takano, K. Hirata, and H. Sakata. Unidirectional electronic structure in the parent state of iron-chalcogenide superconductor $Fe_{1+\delta}Te$. *J. Phys. Soc. Jpn.*, 81:074714, (2012).

23. T. Machida, K. Kogure, T. Kato, H. Nakamura, H. Takeya, T. Mochiku, S. Ooi, Y. Mizuguchi, Y. Takano, K. Hirata, and H. Sakata. Observation of an isosceles triangular electronic structure around the excess iron atoms in $Fe_{1+y}Te$. *Phys. Rev. B*, 87(21):214508, (2013).

24. O. Zachar, S.A. Kivelson, and V.J. Emery. Landau theory of stripe phases in cuprates and nickelates. *Phys. Rev. B*, 57:1422–1426, (1998).

25. A.V. Balatsky, D.N. Basov, and J.X. Zhu. Induction of charge density waves by spin density waves in iron-based superconductors. *Phys. Rev. B*, 82(14):144522, (2010).

26. M. Bode, M. Getzlaff, and R. Wiesendanger. Spin-polarized vacuum tunneling into the exchange-split surface state of Gd(0001). *Phys. Rev. Lett.*, 81:4256–4259, (1998).

27. E. Rodriguez, C. Stock, P. Zajdel, K.L. Krycka, C.F. Majkrzak, F. Charles, P. Zavalij, and M.A. Green. Magnetic-crystallographic phase diagram of the superconducting parent compound $Fe_{1+x}Te$. *Phys. Rev. B*, 84(6):064403, (2011).

28. C. Koz, S. Rößler, A.A. Tsirlin, S. Wirth, and U. Schwarz. Low-temperature phase diagram of $Fe_{1+y}Te$ studied using x-ray diffraction. *Phys. Rev. B*, 88:094509, (2013).

29. J. Zaanen and O. Gunnarsson. Charged magnetic domain lines and the magnetism of high T_c oxides. *Phys. Rev. B*, 40(10):7391, (1989).

30. J.M. Tranquada, B.J. Sternlieb, J.D. Axe, Y. Nakamura, and S. Uchida. Evidence for stripe correlations of spins and holes in copper oxide superconductors. *Nature*, 375:561–563, (1995).

31. S.A. Kivelson, E. Fradkin, and V.J. Emery. Electronic liquid-crystal phases of a doped Mott insulator. *Nature*, 393(6685):550–553, (1998).

32. M. Vershinin, S. Misra, S. Ono, Y. Abe, Y. Ando, and A. Yazdani. Local ordering in the pseudogap state of the high-T_c superconductor $Bi_2Sr_2CaCu_2O_{8+\delta}$. *Science*, 303:1995–1998, (2004).

33. Y. Kohsaka, C. Taylor, K. Fujita, A. Schmidt, C. Lupien, T. Hanaguri, M. Azuma, H. Eisaki, H. Takagi, S. Uchida, and J.C. Davis. An intrinsic bond-centered electronic glass with unidirectional domains in underdoped cuprates. *Science*, 315:1380–1385, (2007).

34. F. Gross, B.S. Chandrasekhar, D. Einzel, K. Andres, P.J. Hirschfeld, H.R. Ott, J. Beuers, Z. Fisk, and J.L. Smith. Anomalous temperature dependence of the magnetic field penetration depth in superconducting UBe_{13}. *Z. Phys. B*, 64:175–188, (1986).

35. D.S. Inosov, J.S. White, D.V. Evtushinsky, I.V. Morozov, A. Cameron, U. Stockert, V.B. Zabolotnyy, T.K. Kim, A.A. Kordyuk, S.V. Borisenko, E.M. Forgan, R. Klingeler, J.T. Park, S. Wurmehl, A.N. Vasiliev, G. Behr, C.D. Dewhurst, and V. Hinkov. Weak superconducting pairing and a single isotropic energy gap in stoichiometric LiFeAs. *Phys. Rev. Lett.*, 104:187001, (2010).

Acknowledgements: We acknowledge discussions with S. Chi, M. Etzkorn, F. Kruger, A.P. Mackenzie, S. Rößler, U. Rößler and M. Ternes. ZS acknowledges financial support from Rubicon grant No. 680.50.1119 (NWO, NL). VT, AL and JD acknowledge financial support from

the DFG Transregional Research Center TRR80 (Augsburg, Munich, Stuttgart). PW acknowledges funding from EPSRC and Max-Planck-Society.

FIG. 1: **Magnetic Order in FeTe and its detection in STM.** (**A**) Schematic illustration of the non-magnetic (dashed lines) and magnetic unit cell (solid lines) of FeTe. The panel to the right shows the expected pattern in a Fourier transformed topographic image due to the top-layer Te atoms, the Fe square lattice and the magnetic order. Axis are in units of $2\pi/a$ and $2\pi/b$ for q_x and q_y, respectively. (**B**) Schematic of spin-polarized STM measurement on FeTe, with a non-magnetic tip which has a small magnetic iron or iron tellurium cluster at its apex. (**C**) topography $z(\mathbf{x})$ of a $\mathrm{Fe}_{1+y}\mathrm{Te}$ sample with $y = 0.08$, acquired with a tip which shows no magnetic contrast, excess iron atoms show up as protrusions ($V_b = 60\ \mathrm{mV}$, $I_t = 200\ \mathrm{pA}$, $T = 3.8\mathrm{K}$). Next to the topography, its Fourier transform $\widetilde{z}(\mathbf{q})$ is displayed, showing the peaks associated with the Te lattice at $\mathbf{q}^a_{\mathrm{Te}} = (\pm 1, 0)$ and $\mathbf{q}^b_{\mathrm{Te}} = (0, \pm 1)$. One pair of peaks, marked $\mathbf{q}_{\mathrm{CDW}}$ ($= \mathbf{q}^a_{\mathrm{Te}}$) shows up with stronger intensity than the other; (**D**) topography acquired in the same place as C with a tip which shows magnetic contrast ($V_b = 60\ \mathrm{mV}$, $I_t = 200\ \mathrm{pA}$, $T = 3.8\mathrm{K}$) with its Fourier transform, showing beside the peaks due to the Te lattice as in B additional ones associated with magnetic order at $\mathbf{q}_{\mathrm{AFM}} = (\pm 1/2, 0)$. (**E**) Ball model of the top-most tellurium and iron atoms with the spin structure determined from neutron scattering overlayed on a topographic image. Arrows on Te atoms indicate spin polarization as obtained from calculations, on iron atoms the local magnetic moment (because the direction of the magnetization of the tip is unknown, a magnetic structure with all spins reversed can yield the same contrast). Image taken at $T = 30\ \mathrm{mK}$, $V_b = 50\ \mathrm{mV}$, $I_t = 500\ \mathrm{pA}$). (**F**) Topographic image of a twin boundary. The stripes in the two domains are perpendicular to each other ($T = 30\ \mathrm{mK}$, $V_b = 150\ \mathrm{mV}$, $I_t = 30\ \mathrm{pA}$).

FIG. 2: **Field dependence of Magnetic Contrast.** (**A**) Topography measured at $3.8\mathrm{K}$ at a magnetic field of $5\mathrm{T}$ in a direction close to the surface normal, (**B**) topography taken in the same place in a magnetic field of $-5\mathrm{T}$ ($V_b = 80\mathrm{mV}$, $I_t = 100\mathrm{pA}$). Images obtained at zero field before the topography in A was measured show the same contrast as the one shown in panel B (see Fig. S4A). (**C**) Upper Panel: Line profile normal to the modulation (averaged along the modulation (parallel to b) in the white box in A and B) showing the change in the modulation with magnetic field, lower panel: difference (red) and average (black) of the two line cuts shown in the upper panel, representing spin polarization and topographic height along the profile. The spin polarization is obtained as described in Suppl. Mat. S2. Vertical dashed lines mark positions of largest positive and negative spin polarization. (**D**) average of the two images in A and B showing the topography as it would be obtained with a non-magnetic tip. (**E**) map of spin polarization obtained from the difference of the two images in A and B. (**F**) upper panel: line cut through a pair of excess iron defects which have different spin-polarization (taken at light-blue solid line in A and B), lower panel: profile of spin polarization (red) and topography (black) along the line cut (light blue solid line in D and E). Vertical dashed lines mark positions of the two excess iron atoms. (**G**) Model of an excess Fe atom on an FeTe layer with the spin-structure deduced from our data. The excess iron atom is marked Fe II. It resides between four tellurium atoms.

FIG. 3: **Temperature dependence of Magnetic Contrast.** (**A**) topography recorded at 54 K. Inset shows the Fourier transform of the topography. The unidirectional modulation is not detected at this temperature ($V_b = 100$ mV, $I_t = 800$ pA). (**B**) Intensity $\Psi_{\mathrm{AFM}} = \widetilde{z}(\mathbf{q}_{\mathrm{AFM}})/\widetilde{z}(\mathbf{q}^b_{\mathrm{Te}})$ at the wave vector of the spin density wave $\mathbf{q}_{\mathrm{AFM}}$ as a function of temperature. Error bars are obtained from the standard deviation from the mean. Solid red line is a fit of mean field theory ($\Psi(T) = \Psi_0 \tanh(\frac{\pi}{2}\sqrt{\frac{T_{\mathrm{c}}}{T} - 1})$ (*34*, *35*)). (**C**) Intensity $\Psi_{\mathrm{CDW}} = (\widetilde{z}(\mathbf{q}_{\mathrm{CDW}}) - \widetilde{z}(\mathbf{q}^b_{\mathrm{Te}}))/\widetilde{z}(\mathbf{q}^b_{\mathrm{Te}})$ at the wave vector of the charge density wave $\mathbf{q}_{\mathrm{CDW}}$ as a function of temperature. The fit in C has been done by fixing T_{c} to the same value as in B.

FIG. 4: **Magnetic Structure at higher excess iron concentration ($y > 0.12$).** (**A**) topography obtained from a sample with high excess iron concentration ($y = 0.15$), showing stripe modulation in two directions superimposed ($V_b = 100$ mV, $I_t = 100$ pA, $T = 1.8$K). A large part of excess iron has been picked up by the tip, leaving an almost clean Te-terminated surface. Inset: Fourier transform of the topography showing peaks associated with magnetic contrast around $(\pm 1/2, 0)$ and $(0, \pm 1/2)$. (**B**) Filtered image showing the components associated with magnetic contrast in different colours to visualize the bidirectional stripe order.

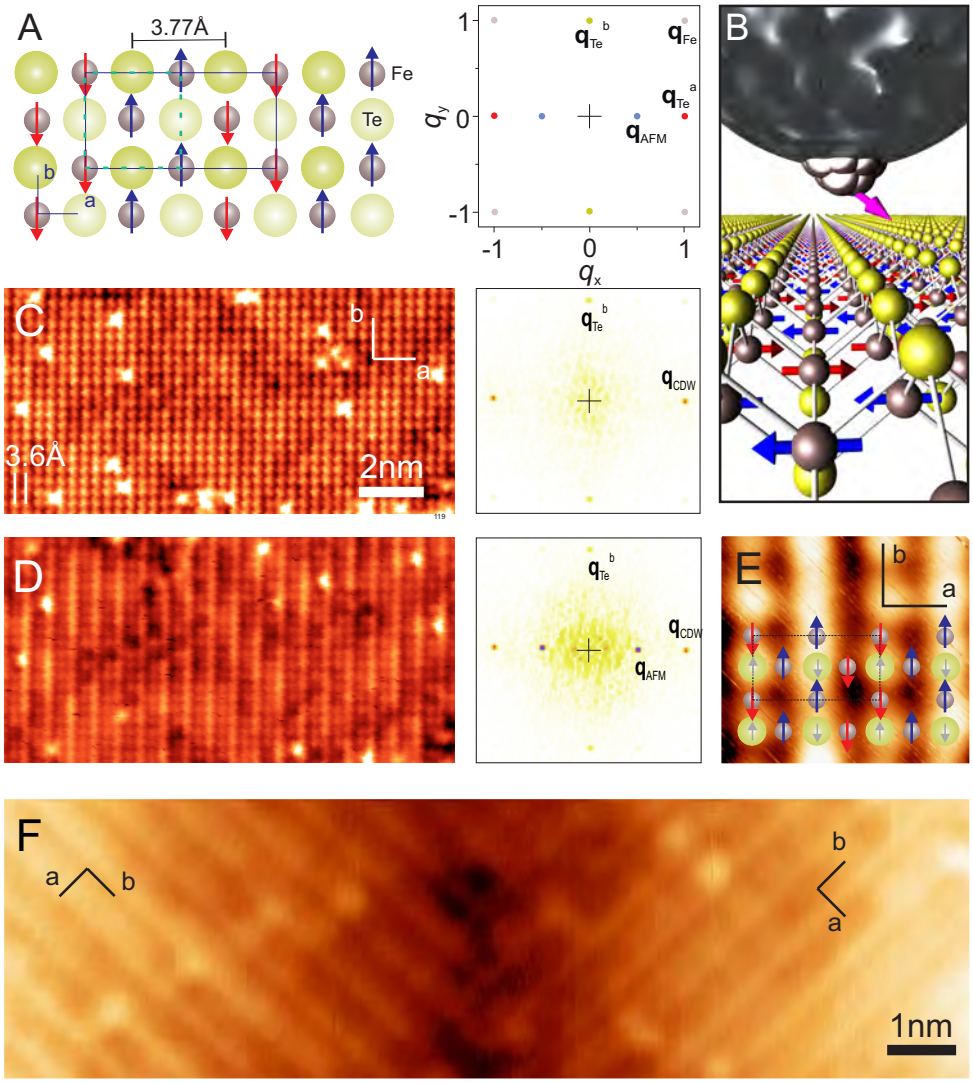
A
3.77Å
Fe
Te
b
a
1
0
-1
q_y
-1
0
1
q_x
q_{Te}^{b}
q_{Fe}
q_{Te}^{a}
q_{AFM}
B
C
b
a
3.6Å
2nm
q_{Te}^{b}
q_{CDW}
D
q_{Te}^{b}
q_{CDW}
q_{AFM}
E
b
a
F
a
b
b
a
1nm

Fig. 1

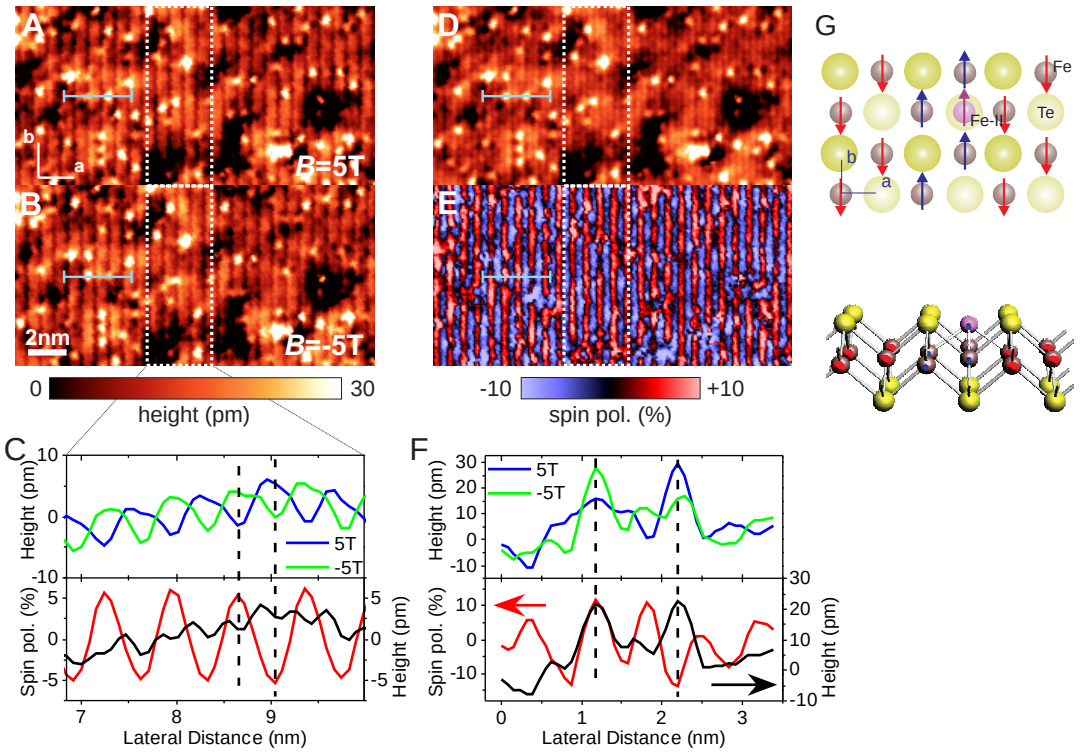
A
B
B=5T
B=-5T
2nm
b
a
0
30
height (pm)
D
E
-10
+10
spin pol. (%)
G
Fe
Te
Fe-II
C
F
Height (pm)
Spin pol. (%)
5T
-5T
Lateral Distance (nm)

Fig. 2

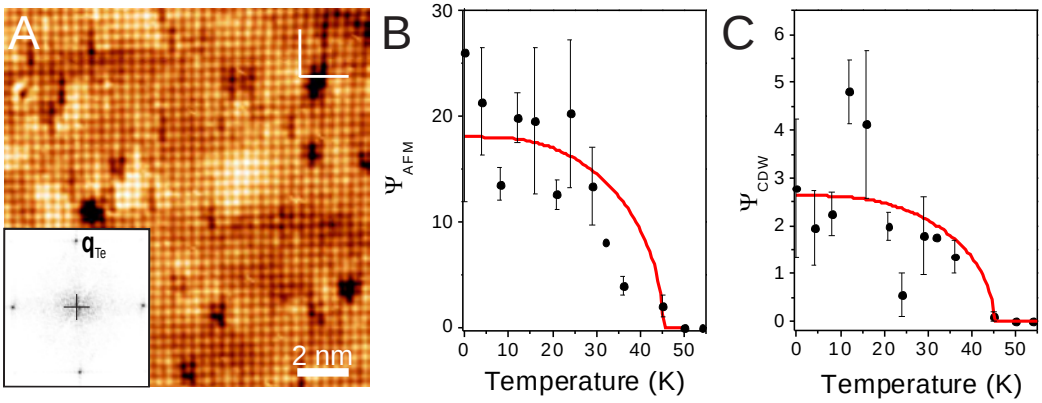

Fig. 3

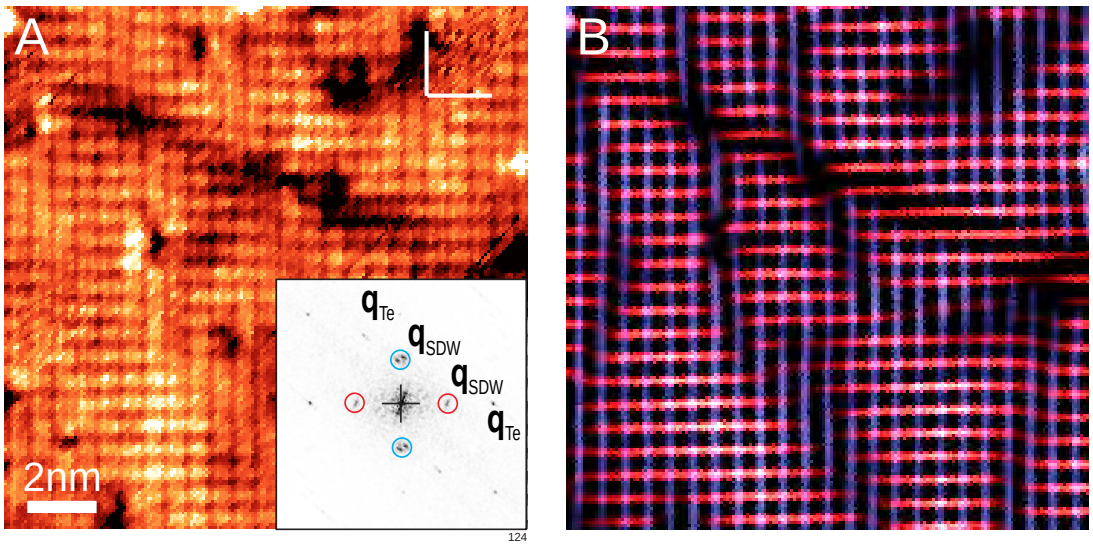

Fig. 4

Supplementary Materials for 'Real Space Imaging of the Atomic-Scale Magnetic Structure of $Fe_{1+y}Te$'

Mostafa Enayat,[1,*] Zhixiang Sun,[1,*] Udai Raj Singh,[1] Ramakrishna Aluru,[1] Stefan Schmaus,[1] Alexander Yaresko,[1] Yong Liu,[1,†] Chengtian Lin,[1] Vladimir Tsurkan,[2,3] Alois Loidl,[2] Joachim Deisenhofer,[2] and Peter Wahl[1,4,‡]

[1]*Max-Planck-Institut für Festkörperforschung, Heisenbergstr. 1, D-70569 Stuttgart, Germany*

[2]*Center for Electronic Correlations and Magnetism, Experimental Physics V, University of Augsburg, D-86159 Augsburg, Germany*

[3]*Institute of Applied Physics, Academy of Sciences of Moldova, MD 2028, Chisinau, R. Moldova*

[4]*SUPA, School of Physics and Astronomy, University of St. Andrews, North Haugh, St. Andrews, Fife, KY16 9SS, United Kingdom*

(Dated: April 29, 2014)

*These authors contributed equally.

†Present address: Division of Materials Sciences and Engineering, Ames Laboratory, US DOE, Ames, Iowa 50011, USA

‡Electronic address: gpw2@st-andrews.ac.uk

S1. MATERIALS AND METHODS

A. Single crystal growth and characterization.

Single crystals of FeTe were grown by the Bridgman technique from high purity (4N) materials (*S1*). Data in the monoclinic phase has been obtained on three samples with different excess iron concentrations of $y = 0.07 - 0.13$ as determined by Energy-dispersive X-ray spectroscopy (EDX) analysis. Superconducting quantum interference device (SQUID) characterization of the magnetization of the samples shows the magnetostructural phase transition between 60 and 67 K. The behavior of the magnetic phase transition as function of excess iron is consistent with the previously published phase diagram (*S2*). The data in Fig. 4 has been obtained on a single crystal with excess iron concentration $y = 0.15$ as determined from EDX and the magnetic phase transition at 62 K measured in SQUID magnetometry. We occasionally observe inhomogeneity in the distribution of the excess iron atoms in STM images, which is likely due to excess iron having been picked up by the tip of the STM (see, e.g., Fig. 4A - which shows only very little excess iron despite a concentration of $y = 0.15$).

In samples with excess iron concentration $y < 0.12$, the monoclinic distortion of the lattice can be detected as a slight difference in the positions of the atomic peaks, further, due to the monoclinic distortion, boundaries between different domains reveal a surface angle, as shown in Fig. 1F. The tilt angle between the two surfaces is 1.46°, close to what is expected from X-ray diffraction (*S3*).

B. STM Experiments

Experiments were performed in two home-built low temperature STMs, one operating at temperatures down to 10 mK (*S4*) and one with a base temperature of 1.5 K (*S5*), both in cryogenic vacuum. Samples are prepared by *in-situ* cleaving at low temperatures. We used STM tips cut from PtIr and Vanadium wire, which have subsequently been prepared by field emission on a Au(111) single crystal (Vanadium tips did not show a superconducting gap anymore after sufficient field emission). Bias voltages are applied to the sample, with the tip at virtual ground.

Prior to performing experiments on $Fe_{1+y}Te$ samples, we performed field emission on a gold single crystal. After inserting the $Fe_{1+y}Te$ samples into the STM head, tips have been prepared either by soft indentation into the sample, picking small clusters of FeTe up, and/or scanning at large current or small bias voltage to collect excess Fe atoms from the surface. Pick-up of clusters of FeTe usually results in nanometer sized holes in the surface. The majority of images obtained following either one of the tip preparation methods show magnetic contrast. Images shown in fig. 1D and fig. 2A, B have been taken with a tip following pick-up of excess iron atoms only.

C. Magnetic Field

Magnetic fields are applied normal to the sample surface, negative fields point along the surface normal. While it is surprising that at a magnetic field of 5T normal to the surface, we can still detect magnetic contrast, there are likely a number of factors enabling this:

- Shape anisotropy of the magnetic cluster at the tip: if, e.g., its easy axis is at $\sim 45°$ to the field direction, the magnetization of the tip will still maintain an (albeit small) in-plane component even under 5T out-of-plane field (see, e.g., Ref. (*S6*) for parameters for iron nanoparticles).
- Magnetocrystalline anisotropy: the chemical composition of our tip apex is only rather poorly known, there are materials with large spin-orbit coupling (Au, Pt, Ir, potentially Te) which could induce a sizeable magnetocrystalline anisotropy
- Due to a small tilt in the surface (for images in fig. 2 on the order of $3°$ in the direction of the stripes), the magnetic field is not exactly normal to the surface, but has a small in-plane component with respect to the magnetic structure.

D. Data processing

1. Topographies

Topographies shown in the manuscript show raw data, apart from a rotation to align the lattice in the same way for each figure and subtraction of a plane from the data. In some

cases, line average have been subtracted to remove non-linear backgrounds. Topographies shown in fig. 1 and 2 have been cropped from larger topographies (see fig. S1). Topographic images analyzed for the temperature dependence shown in Fig. 3B and C have been taken with bias voltages between 100mV and 300mV.

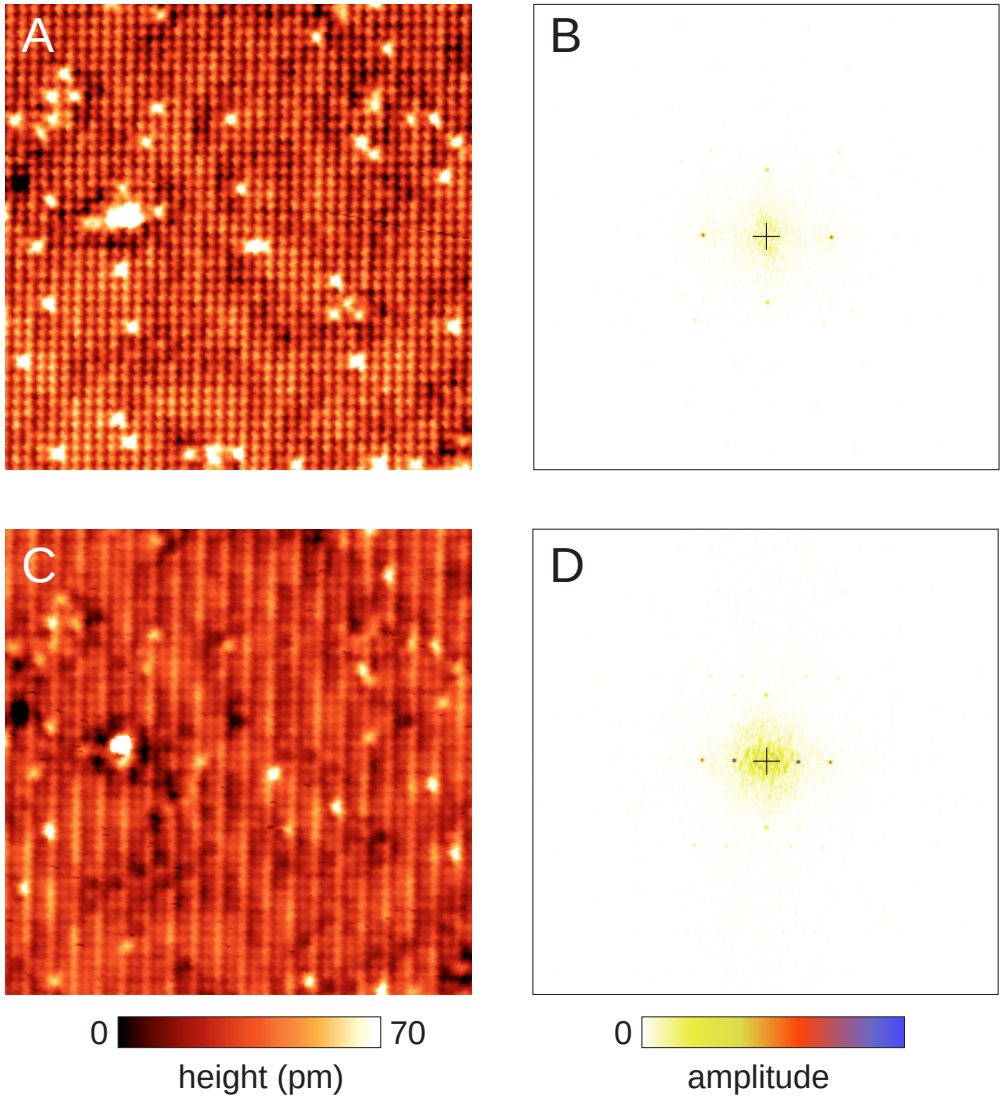

FIG. S1: **Topography with and without magnetic contrast.** (**A**) Topography without magnetic contrast and (**B**) corresponding Fourier transform. (**C**) topography with a tip showing magnetic contrast in same field of view as A. (**D**) Fourier transform of C. The images shown in fig. 1C and D have been cropped from the ones shown here. A and C are shown with the same height scale, for B and D the intensity scale has been adjusted to match the colour scheme in Fig. 1A ($V_b = 60$ mV, $I_t = 200$ pA, $T = 3.8$K, image size: $13.9 \times 13.9\text{nm}^2$).

2. Fourier Transforms

Images showing Fourier Transforms show the modulus of the amplitude of the Fourier components, using a Bartlett (or triangular) window function to reduce edge effects. The Fourier transforms in Fig. 1C, D have been cropped to highlight the main features, the full scale Fourier Transforms are shown in Fig. S1. The only further processing applied to the Fourier transforms is adjusting the colour scale, which has been done to make the colours match the colours in the schematic of the Fourier transform in fig. 1A.

E. DFT calculations

Spin-polarized band structure calculations were performed in the local spin density approximation (LSDA) using the Perdew-Wang (*S7*) parameterization for the exchange-correlation potential. The linear muffin-tin orbital (LMTO) method (*S8*) was used. Details of the implementation of the LMTO method can be found in Ref. (*S9*). We used the experimental monoclinic low temperature crystal structure of $Fe_{1.076}Te$ (*S10*) but neglected the small excess of Fe(2) ions. In agreement with the neutron scattering data the lowest total energy for bulk FeTe was found for double-stripe magnetic order with the ordering vector $(1/2, 0, 1/2)$ and the Fe spin moment of $2\mu_B$ directed along the b axis, i.e., along ferromagnetic (FM) Fe chains.

1. Slab Calculation

Surface effects were simulated by performing calculations for a slab in which two consecutive FeTe layers in a $1 \times 1 \times 8$ supercell of the monoclinic $P2_1/m$ structure were replaced by empty spheres. No attempt to relax atomic positions at the surface was made. For simplicity we considered the double-stripe magnetic order in the ab plane and FM order along the c axis of the slab. A half of the slab is shown in Fig. S2a. The key result is that there is substantial spin polarization on the tellurium atoms, hence if the tip is spin-polarized, magnetic contrast can be expected even if there was no contribution from direct tunneling to the Fe d-orbitals to the current. The spin polarization at the Fermi level on Fe and Te atoms with opposite magnetization has the same polarity, as it is due to minority electrons on Fe and due to majority electrons on Te.

The term spin-polarization used in the main manuscript in the context of the calculations refers to the spin-polarization of electrons at the Fermi edge, i.e. $\frac{\rho_\downarrow(E_\mathrm{F})-\rho_\uparrow(E_\mathrm{F})}{\rho_\downarrow(E_\mathrm{F})+\rho_\uparrow(E_\mathrm{F})}$. For spin-polarized tunneling the spin-polarizations as given in the figures S2 and S3 can give a rough estimation only of whether or not a magnetic contrast can be expected - because the spin-polarization of the current will sensitively depend on the overlap with tip states.

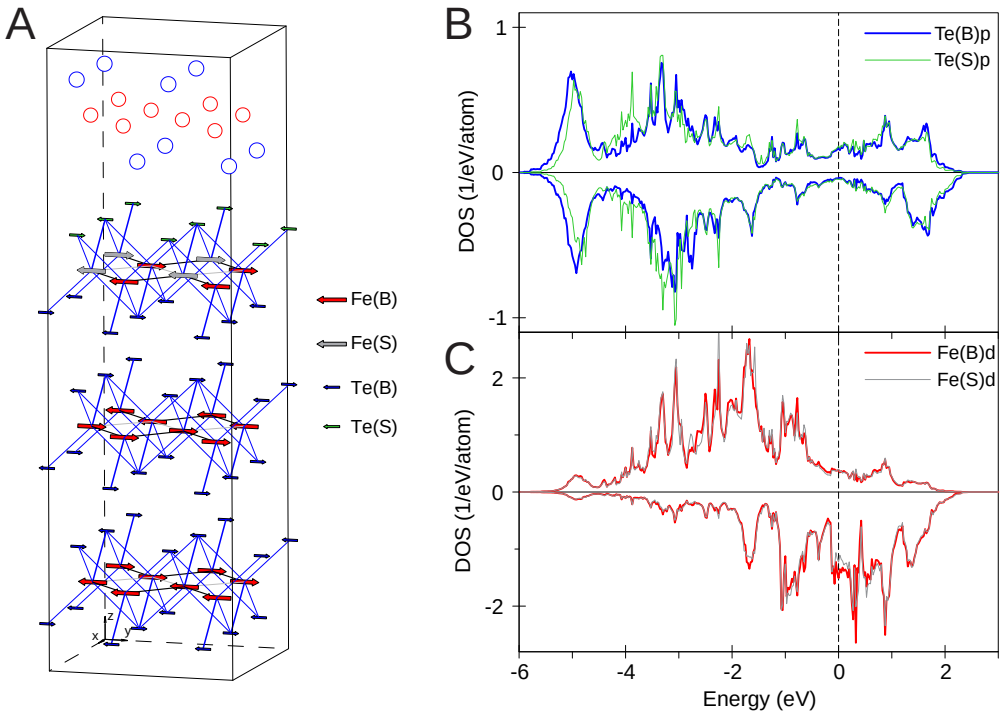

FIG. S2: **DFT calculations** (**A**) Slab used for DFT calculations with magnetic structure obtained drawn on top. As can be seen the spin on Te atoms is opposite to the three nearest Fe atoms. (**B**) Projected spin-resolved density of states (PDOS) for Te *p*-states, green solid curve is for Te atoms on the vacuum side of the iron layer, blue solid line for the Te atoms on the bulk side. (**C**) PDOS for Fe *d* states, with grey solid curve showing the PDOS for Fe atoms whose nearest neighbour Te atom is at the surface and red where it is on the bulk side. (the Fe-Te bonds are not all the same length due to the monoclinic distortion, the bond to the nearest Te atom is indicated by a slightly thicker blue line for each Fe atom). It can be clearly seen that substantial spin-polarization near the Fermi level exists not only for the Fe states, but also for the Te states. The Te *p*-states exhibit a spin-polarization of $\sim 60\%$ at the Fermi energy, the Fe *d* states of $\sim 52\%$.

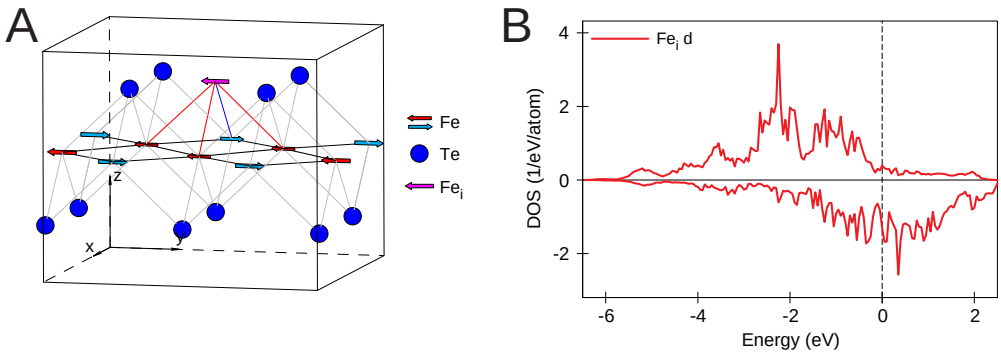

FIG. S3: **Magnetic Coupling of Excess Fe Impurities** (**A**) Supercell used to calculate the coupling of excess iron impurities to the iron square lattice. The calculation has been performed with the spin on the excess iron impurity either parallel or antiparallel to the three equal-spin nearest-neighbour iron atoms, yielding an energy difference of 140meV favouring ferromagnetic coupling. This rather strong coupling also explains why the magnetic field does not change the magnetization of the excess Fe impurities. (**B**) Spin-polarized density of states at the excess Fe atom. Excess iron atoms have a spin-polarization of $\sim 53\%$.

2. Impurity Calculation

We have performed calculations for an interstitial Fe impurity, placing it at the position determined previously by X-ray diffraction (see EPAPS of Ref. *S10*), the supercell is shown in fig. S3A. The projected density of states is displayed in fig. S3B. The calculations yield a strong ferromagnetic coupling of the spin of the excess iron atoms to the three equal-spin nearest-neighbour iron atoms in the iron square lattice, with the ferromagnetic spin alignment with the three equal-spin neighbours being $\sim$ 140meV more favorable than antiferromagnetic alignment.

S2. EXTRACTING THE SPIN-POLARIZATION

From the height difference Δz between equivalent sites of opposite magnetization, the spin polarization of the tunneling current can be obtained from (*S11*)

$$P(\Delta z, \kappa) = \frac{e^{\kappa \Delta z} - 1}{e^{\kappa \Delta z} + 1} \tag{S1}$$

With a work function of $\Phi_s \approx \Phi_t \approx 5$eV (and $\kappa = 2\sqrt{\frac{m}{\hbar^2}(\Phi_t + \Phi_s)}$) and a height difference of up to 20pm, we obtain a spin-polarization of the tunneling current of up to 25%. Assuming

a spin-polarization of the tip states of 44% which has been obtained for iron coated tungsten tips (*S12*), the polarization in the surface is up to $\sim 50\%$. This provides only a rough estimate, as our tips are now coated with a thin layers of iron, but will have some irregularly shaped iron cluster, in some cases with FeTe, at their apex.

Using a Taylor expansion for $e^{\kappa\Delta z}$ to first order, we obtain

$$P(\Delta z, \kappa) \approx \frac{\kappa}{2}\Delta z. \tag{S2}$$

This is valid for $\kappa\Delta z \ll 1$. For typical work functions, $\kappa \sim 2.3\text{Å}^{-1}$, and height differences of 20pm between oppositely polarized regions, the error stays well below 5% of the spin polarization. Therefore the height difference between images obtained with a tip with opposite spin polarization in the same place is proportional to the spin polarization of the current. Knowledge of κ as extracted from Fig. S4E allows us to generate a map of the spin polarization as shown in Fig. 2E.

S1. X. Liu, C.C. Lee, Z.J. Xu, J.S. Wen, G. Gu, W. Ku, J.M. Tranquada, and J.P. Hill. X-ray diffuse scattering study of local distortions in $Fe_{1+x}Te$ induced by excess Fe. *Phys. Rev. B*, 83(18):184523, (2011).

S2. S. Rößler, D. Cherian, W. Lorenz, M. Doerr, C. Koz, C. Curfs, Y. Prots, U.K. Rößler, U. Schwarz, S. Elizabeth, and S. Wirth. First-order structural transition in the magnetically ordered phase of $Fe_{1.13}$ Te. *Phys. Rev. B*, 84(17):174506, (2011).

S3. S. Li, C. de la Cruz, Q. Huang, Y. Chen, J.W. Lynn, J. Hu, Y.L. Huang, F.C. Hsu, K.W. Yeh, M.K. Wu, and P. Dai. First-order magnetic and structural phase transitions in $Fe_{1+y}Se_xTe_{1-x}$. *Phys. Rev. B*, 79:054503, (2009).

S4. U.R. Singh, M. Enayat, S.C. White, and P. Wahl. Construction and performance of a dilution-refrigerator based spectroscopic-imaging scanning tunneling microscope. *Rev. Sci. Instr.*, 84: 013708, (2013).

S5. S.C. White, U.R. Singh, and P. Wahl. A stiff scanning tunneling microscopy head for measurement at low temperatures and in high magnetic fields. *Rev. Sci. Instr.*, 82:113708, (2011).

S6. S. Wirth, M. Field, D.D. Awschalom, and S. von Molnár. Magnetization behavior of nanometer-scale iron particles. *Phys. Rev. B*, 57:14028, (1998).

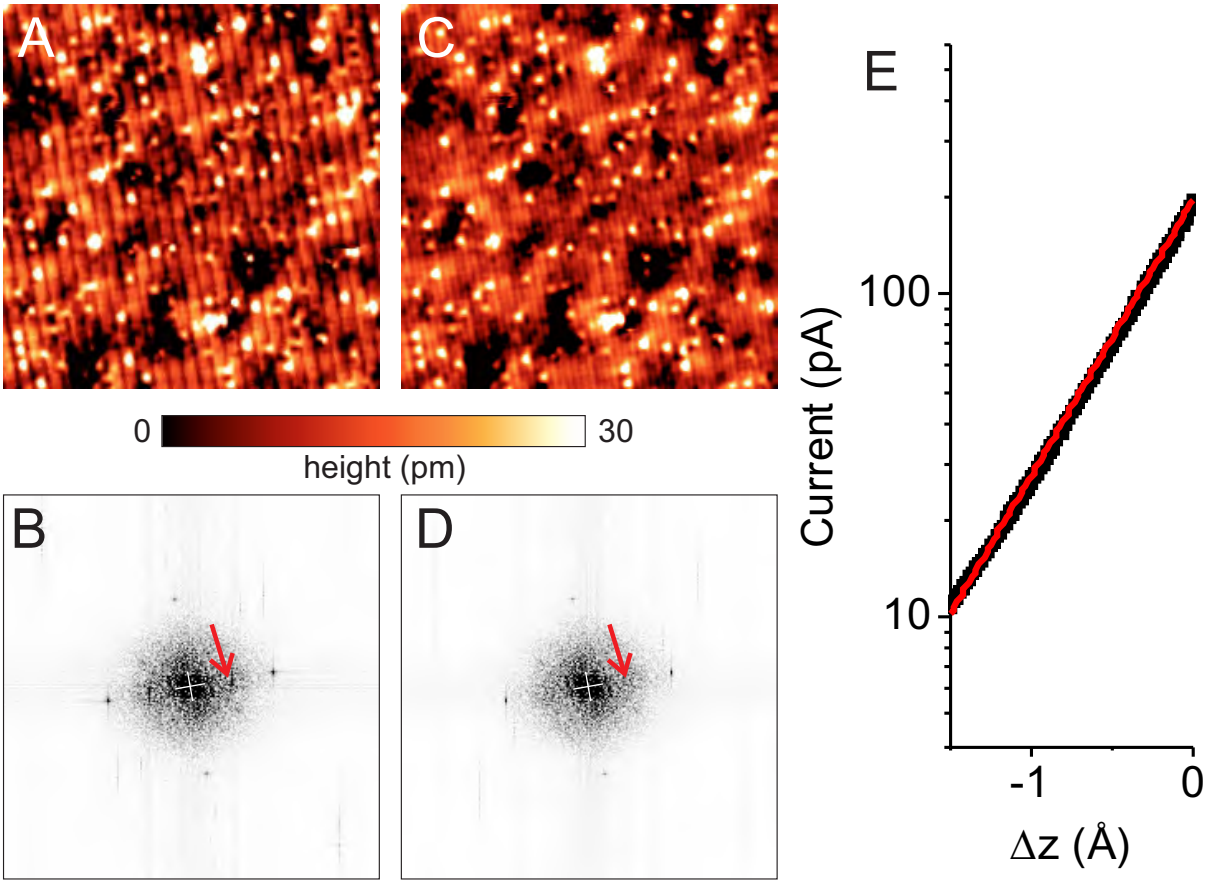

FIG. S4: **Magnetic field dependence.** (**A**) Topography taken in the same place as Fig. 2A, B at zero field ($40 \times 40\text{nm}^2$, $V_b = 80\text{mV}$, $I_t = 200$ pA, $T = 3.8$ K); (**B**) Fourier transform, the peak associated with magnetic order is marked by an arrow; (**C**) large scale image from which the one in Fig. 2D has been extracted; (**D**) Fourier transform of C showing that the peak associated with magnetic order (the position is marked by an arrow) is gone (though in some places hints of the magnetic contrast can still be seen, due to not perfect alignment). Height scale for A and C is the same as in Fig. 2A, B, D; (**E**) I_t-Δz curve for the same tip which was used to acquire topographies in A and Fig. 2A, B, to extract κ - allowing to obtain quantitative information about the spin polarization of the tunneling current. The fit (red solid line) is for $a \exp(\kappa \Delta z)$, yielding $\kappa = 1.97\text{Å}^{-1}$ (corresponding to $\Phi_s + \Phi_t = 7.41\text{eV}$, see section S2). Δz is the change of tip-sample distance relative to the tunneling setpoint at $V_b = 80\text{mV}$ and $I_t = 200\text{pA}$.

S7. J.P. Perdew and Y. Wang. Accurate and simple analytic representation of the electron-gas correlation energy. *Phys. Rev. B*, 45:13244–13249, (1992).

S8. O. K. Andersen. Linear methods in band theory. *Phys. Rev. B*, 12:3060, (1975).

S9. V. Antonov, B. Harmon, and A. Yaresko. *Electronic structure and magneto-optical properties of solids*. Kluwer Academic Publishers, Dordrecht, Boston, London, (2004).

S10. W. Bao, Y. Qiu, Q. Huang, M.A. Green, P. Zajdel, M.R. Fitzsimmons, M. Zhernenkov, S. Chang, M. Fang, B. Qian, E.K. Vehstedt, J. Yang, H.M. Pham, L. Spinu, and Z.Q. Mao. Tunable ($\delta\pi$, $\delta\pi$)-type antiferromagnetic order in α-Fe(Te, Se) superconductors. *Phys. Rev. Lett.*, 102(24):247001, (2009).

S11. R. Wiesendanger, H.-J. Güntherodt, G. Güntherodt, R.J. Gambino, and R. Ruf. Observation of vacuum tunneling of spin-polarized electrons with the scanning tunneling microscope. *Phys. Rev. Lett.*, 65:247–250, (1990).

S12. M. Bode, M. Getzlaff, and R. Wiesendanger. Spin-polarized vacuum tunneling into the exchange-split surface state of Gd(0001). *Phys. Rev. Lett.*, 81:4256–4259, (1998).

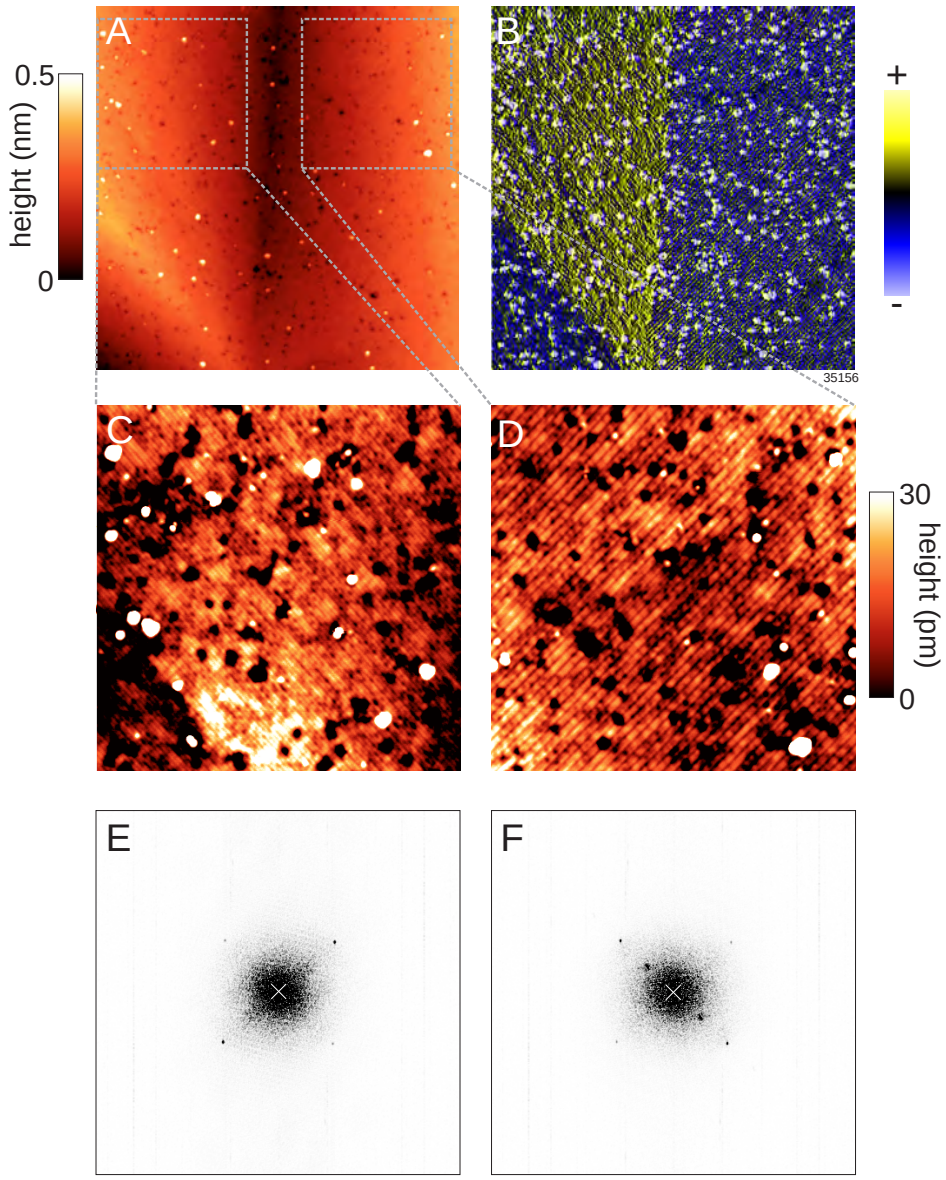

FIG. S5: **Imaging of different domains** (**A**) Topography across two different domains, acquired with a tip where the spin polarization is in-plane, coincidentally parallel to the spin-polarization in the right part of the topography ($61 \times 61\text{nm}^2$), (**B**) is a derivative in the horizontal direction of the topography to better visualize the modulation in the two domains. (**C**, **D**) images cut out from the topography in A in the two different domains, left and right respectively as indicated by red squares ($25 \times 25\text{nm}^2$). The magnetic contrast can only be clearly seen in D. This is also evidenced in the FFTs of C and D, shown in (**E**) and (**F**): only in F the modulation at $\mathbf{q}_{\text{AFM}}$ shows up, while the one at $\mathbf{q}_{\text{CDW}}$ can be seen in both domains. The tip has sufficient resolution to yield atomic resolution and resolve the CDW in both domains with similar intensity, so the different contrast at $\mathbf{q}_{\text{AFM}}$ is not a consequence of tip shape or sharpness (E, F are shown with the same intensity scale).